ORIGINAL PAPER

Centrifuge Modeling and Piv Analysis of Geogrid Reinforced Pile Supported Embankments over Soft Clay

B. Reshma[1] · **B. V. S. Viswanadham**[2] · **K. Rajagopal**[3]

Abstract

Basal reinforcement of embankments and supporting with piles is one of the most recent solutions for rapid embankment construction on soft foundation soils. This paper uses the Particle Image Velocimetry (PIV) to evaluate the performance of unreinforced and reinforced embankments over soft foundation soils in terms of maximum settlement at the embankment base, lateral displacements of the embankment toe and the strains in the reinforcement layer using the digital images captured during the centrifuge model tests at 40*g*. The reinforcement consisted of a single layer of a scaled-down model basal geogrid and additional support from end-bearing or floating piles. The paper examines the effect of varying embankment heights on the geogrid strains and deformation characteristics of subsoil under rapid embankment construction over unreinforced and reinforced soft foundation soil with varying support conditions. The unsupported reinforced embankments showed a peak geogrid axial strain near the toe, whereas it peaked near the mid-section of the embankment for pile supported reinforced embankments. The study also investigates the failure mechanisms of unreinforced and reinforced embankments, with and without pile support, using shear strain contours derived from PIV analysis. The paper underscores the efficacy of PIV as a tool for visualising the deformation behaviour and failure mechanisms in soil during centrifuge model studies. Additionally, the research provides insights into the operation of an in-flight sand hopper used for embankment construction in centrifuge model studies. Post-investigation studies contribute to understanding the potential failure mechanisms in embankments supported by end-bearing and floating piles. Overall, this paper showcases the practical application of PIV in studying the challenges related to rapid embankment construction on soft foundation soils.

Keywords Geogrid · Embankments · Soft foundation soil · Geogrid · Piles · Centrifuge model tests · Particle image velocimetry

Introduction

Specific site conditions, project requirements and budget constraints necessitate constructing embankments in a single stage to minimise delays in construction. Large displacements follow rapid embankment construction on soft soils. Stability, large total and differential settlements are important challenges when constructing embankments in a single stage over soft soil. One of the techniques adopted for rapid construction in soft soils is the geogrid reinforced pile supported embankments (GRPSE), as shown in Fig. 1. Providing a geogrid reinforcement at the base proved to be an effective method to restrain lateral movement, replacing the raker or inclined piles at the embankment toe. The piles supporting the embankments can be end-bearing or floating piles. It finds applications in many highway and railway projects [1, 2]. The embankment load is transferred directly

✉ B. V. S. Viswanadham
viswam@civil.iitb.ac.in

B. Reshma
reshmabsekhar@gmail.com

K. Rajagopal
gopalkr@faculty.iitm.ac.in

1 Department of Civil Engineering, Indian Institute of Technology Madras, Chennai 600 036, India

2 Department of Civil Engineering, Indian Institute of Technology Bombay, Mumbai 400076, India

3 Department of Civil Engineering, Andhra University College of Engineering, Visakhapatnam 530 003, India

Fig. 1 Schematic representation of GRPSE
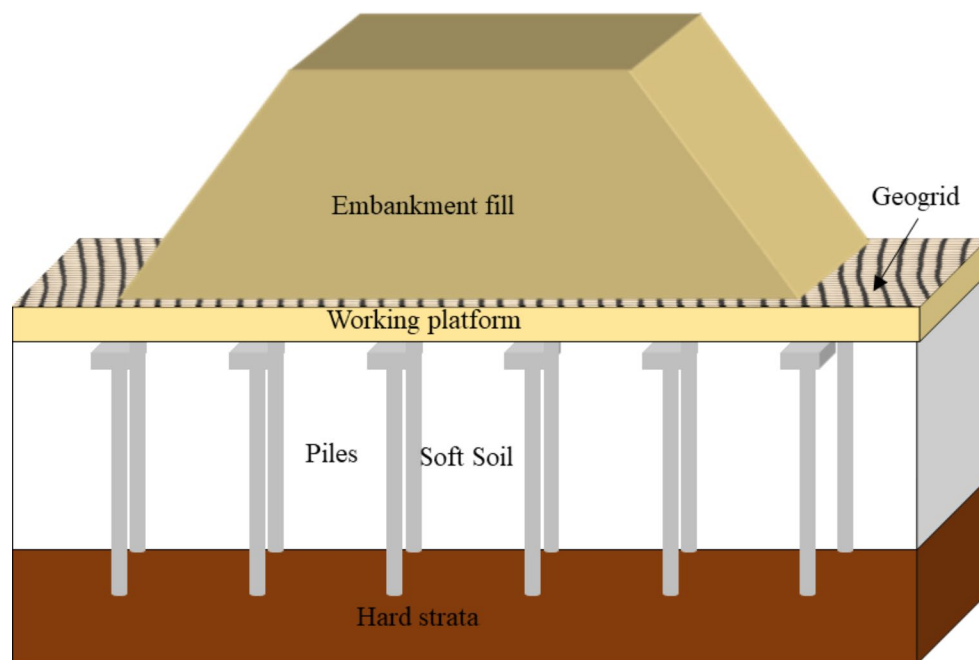
to the piles through geogrid reinforcement (GR) via arching and tensioned membrane effect and the remaining small component to the subsoil [3, 4]. The current design guidelines for GRPSE are BS 8006-1 [5], EBGEO [6], NGG [7], and CUR226 [8]. The parameters in these guidelines differ due to the different assumptions made in the load transfer mechanism.

Many studies have shown that the pile-supported embankments fail due to deep-seated instability and large displacements of the soft ground [9, 10]. Most design codes do not include the estimation of surface displacements [2]. Differential settlements can affect the rideability of the bridge approach slabs, and the lateral movements affect the stability and performance of the piles near the toe of the embankment [10–12]. Hence, it is important to evaluate the serviceability behaviour of reinforced embankments over soft clays.

Due to the expense of conducting full-scale field studies [1, 13–17], many researchers [18–20] have resorted to small-scale laboratory tests to understand the performance of embankments over soft soil. However, small-scale testing at normal gravities does not follow the same stress path and replicate the same stress-strain behaviour as that experienced by the foundation soil. The centrifuge model studies are widely used in geotechnical engineering to solve complex soil-structure interaction problems and capture the true stress-strain behaviour of soil in the field. This study utilises centrifuge modelling techniques to investigate the behaviour of unreinforced and reinforced embankments over soft clays supported by geogrid reinforcement and piles of different bearing types. By replicating stress states similar to those in the prototype but on a smaller scale within a controlled environment at increased gravity levels, the research aims to comprehend the performance of these structures effectively. Many researchers have conducted centrifuge model studies on basal geogrid and pile supported embankments with or without subsoil [21–26]. Previous studies have simulated embankment loading by either applying water pressure from a reservoir, such as in the mobile tray device [21, 22, 27], or by constructing the embankment under normal gravitational conditions and then subjecting it to higher gravitational forces [24, 28–30]. In that case, geostatic stress conditions are not simulated, and the soil is subjected to a different stress state compared to that of the prototype. The embankment loading induces a decrease in effective stress under undrained loading leading to movement along the yield surface towards the critical state line (CSL) before failure. Laboratory modelling at 1 g results in lower stress compared to field conditions, with differences in yield surface dimensions and failure stress. Preparing the embankment model at normal gravity and subjecting it to high gravity aligns failure stress with field conditions but follows a distinct stress path. Inflight embankment construction mimics field conditions, exhibiting a stress path akin to the prototype. Thus, the current centrifuge model study focuses on inflight construction for comprehensive analysis. An inflight sand pourer was developed by Davies [31], where the device had several compartments to store the sand, and the hopper valves were operated in-flight to release the sand. Other researchers who worked on inflight embankment construction or inflight sand pouring are [32–36]. Detert [37] developed a device for inflight stage

construction of the embankment. The inflight sand hopper used in the current study was developed by Hussain [38].

During the past few years, Digital Image Correlation (DIC) [also known as the digital speckle correlation method (DSCM), texture correlation, computer-aided speckle interferometry (CASI) and electronic speckle photography (ESP)] techniques have been increasingly used to understand the deformations and displacements of subsoil in centrifuge modelling. One of the first reported uses of imaging techniques in soil deformation measurement was by [39]. The application of DIC in geotechnical engineering for 1 *g* tests is given by [40–44], and for centrifuge tests is given by [45–50]. The accuracy of displacement measurements taken using image-correlation analysis strongly depends on the surface contrast of the soil, the quality of the images, and the effectiveness of the analysis algorithm.

This paper uses Particle Image Velocimetry (PIV) to evaluate the performance of unreinforced and reinforced embankments over soft foundation soil in terms of maximum settlement at the embankment crest and toe, differential settlements, lateral displacements of the embankment toe and the geogrid strains using the digital images captured during the centrifuge model tests at 40*g* [51]. presented the details of modelling considerations, model materials and procedure of the centrifuge tests conducted with details of the results from instrumentation (LVDT (Linear Variable Differential Transducer data)), displacement vectors, vertical and horizontal displacement contours from GeoPIV_RG software [52]. This research focuses on the variations in geogrid strain concerning both spatial and temporal dimensions across diverse ground improvement methodologies. Within this context, the investigation delves into the intricacies of failure mechanisms by scrutinising horizontal displacement contours and shear strain contours. Furthermore, an investigation is performed to find the distinctive deformation profiles resulting from support by end-bearing and floating piles. Additionally, the paper meticulously outlines the post-investigation studies, shedding light on the potential failure mechanisms inherent in pile-supported embankments. The study focuses on the short-term stability of embankments over soft clays due to the heightened criticality of undrained response in causing slope failure. Rapid changes in pore water pressure and shear strength under undrained conditions pose significant risks to embankment stability and excessive settlement, warranting focused investigation into short-term stability behaviour.

Experimental Procedure

Four sets of tests were carried out on inflight embankment construction over soft soil using a 4.5 m radius large beam centrifuge at the National Geotechnical Centrifuge facility, IIT Bombay. The specifications of the centrifuge equipment are discussed by [53]. These tests aimed to investigate the response of the subsoil in both unreinforced and reinforced support scenarios. The schematic representation of all the centrifuge tests for the present study is shown in Fig. 2. The methodologies proposed by [54–56] form the basis for scaling considerations when modelling soil and geogrid reinforcement in centrifuge tests. The similitude in modelling geogrid involves scaling the tensile load-strain relationship while ensuring consistent frictional bond characteristics. A pivotal aspect is determining the geometric attributes of the model geogrid, achieved through reducing the cross-sectional area of ribs per unit length in both longitudinal and transverse orientations. Maintaining equivalence in frictional bonding necessitates similarity in the soil-geogrid interface friction angle and the proportion of the opening area. The soil-geogrid friction angle remains unchanged. The scaling factor for tensile strength and secant stiffness is calculated by dividing these parameters by a factor of $1/N$ relative to the prototype geogrid values. The similitude in modelling tensile strength and percentage open area of geogrid is as follows:

$$\frac{(T_r)_m}{(T_r)_p} = \frac{\epsilon_m E_g (A')_m}{\epsilon_m E_g (NA')_m} = \frac{1}{N} \tag{1}$$

$$f_o = \left(\frac{a_l a_t}{(a_l + b_l)(a_t + b_t)} \right)_m = \left(\frac{a_l a_t}{(a_l + b_l)(a_t + b_t)} \right)_p \tag{2}$$

where T_r is the tensile strength of geogrid, ε_m is the strain in the geogrid, E_g is the Elastic modulus of geogrid, A' is the rib cross-sectional area, f_o is the percentage open area, a is the grid opening size, b is the width of the rib, N is the scale factor. The subscripts '*m*', '*p*', '*l*' and '*t*' denotes model, prototype, longitudinal direction, and transverse direction respectively.

The similitude in modelling piles can be obtained by ensuring correct axial stiffness (*AE*) and bending stiffness (*EI*) as the prototype. To achieve this, the model pile wall thickness is adjusted to reach the required axial and bending stiffness values that replicate the correct pile section in the prototype. The similitude in axial stiffness and bending stiffness for modelling piles is as follows:

$$E_m \frac{\pi}{4} \left((d_o)_m^2 - (d_i)_m^2 \right) = E_p \frac{1}{N^2} \frac{\pi}{4} \left((d_o)_p^2 - (d_i)_p^2 \right) \tag{3}$$
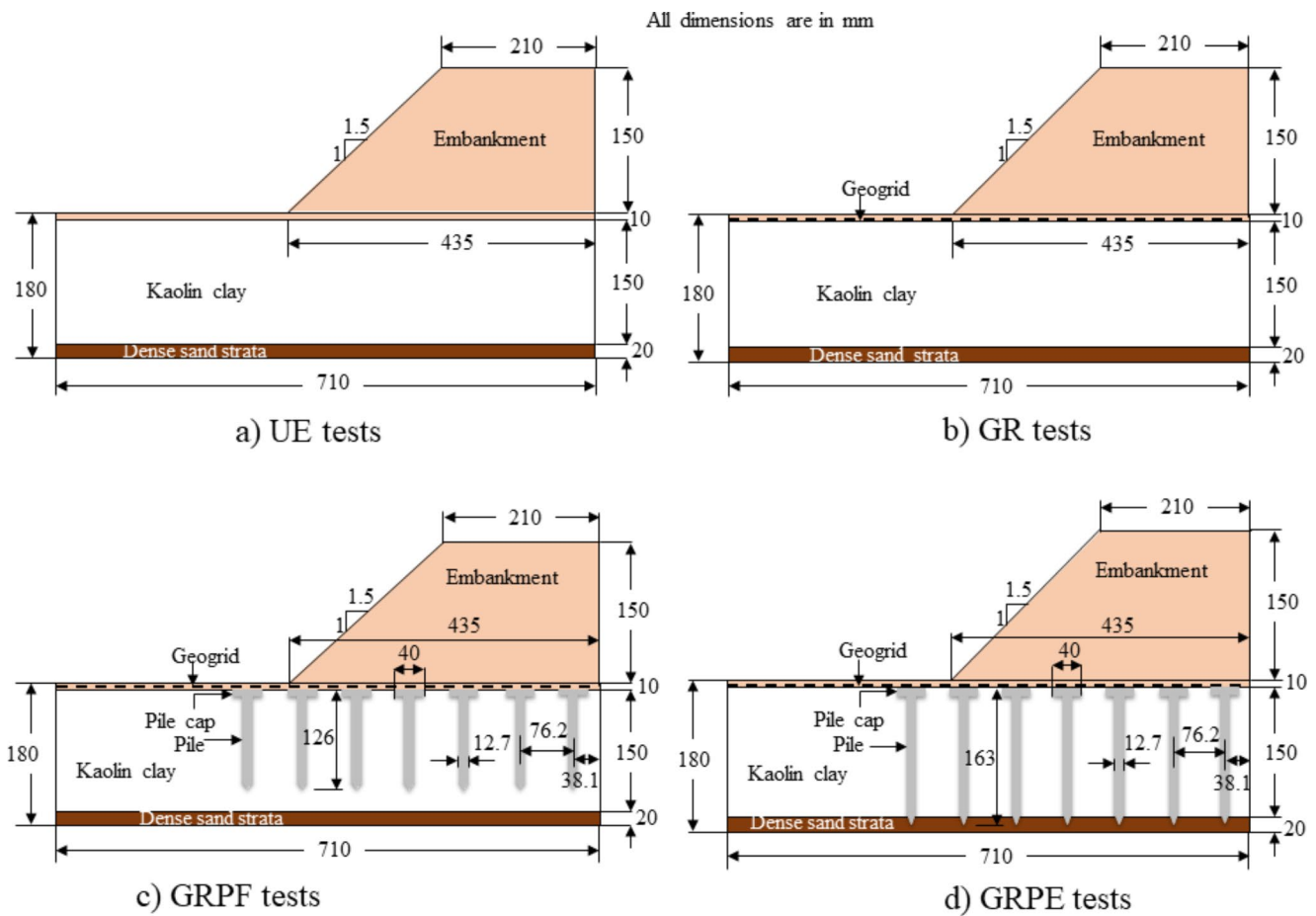
Fig. 2 Schematic representation of all the centrifuge tests

$$E_m \frac{\pi}{64} \left((d_o)_m^4 - (d_i)_m^4 \right) = E_p \frac{1}{N^4} \frac{\pi}{64} \left((d_o)_p^4 - (d_i)_p^4 \right) \qquad (4)$$

where E is the elastic modulus of pile material, d_o is the outer diameter of the pile, d_i is the inner diameter of the pile.

The strong box used in the present study is 760 mm in length, 200 mm in breadth and 410 mm in depth internally. The front wall is provided with a 100 mm thick Perspex sheet for viewing the model during all stages of the centrifuge test at high gravities. In order to achieve plane strain conditions, the front and rear walls are lubricated with white petroleum grease and provided with thick polyethene sheet strips to reduce boundary effects.

The subsoil consisted of a 150 mm thick clay bed made of kaolin soil with an undrained shear strength of 10 kPa placed on a stiff sand layer of 20 mm thickness. The clay employed in this research was procured commercially (liquid limit (LL)=46%, plastic limit (PL)=21%). The fully saturated soil was arranged in layers of 30 mm thickness. Initially, each layer underwent manual packing, followed by compression with a template to eliminate any trapped air.

Considering that all tests were conducted under soft consistency conditions, characterised by a consistency index (I_c) less than 0.3 (where I_c = (LL - Water content)/(LL - PL)), the process of placing the soil and achieving a uniform fill was straightforward. Subsequent to preparing the clay bed, a surcharge of 5 kPa was applied to the entire bed for approximately 24 h to facilitate equilibration as described in [57].

The artificial seeding of black fibres cut to 1 mm × 1 mm was spread on the clay surface to get displacements through particle image velocimetry techniques, as described by Click or tap here to enter text [50]. This was done by tilting the model and removing the front Perspex sheet. The soft soil was then reinforced with hollow aluminium tubes, which simulated piles of different lengths of outer diameter 12.7 mm placed in a square pattern at 6 d spacing at normal gravity, where d is the outer diameter of the pile. The piles were installed at normal gravity by vertically driving through a guide beam, which is akin to the construction of a bored pile in a field [58]. A single layer of model geogrid was placed sandwiched within a 20 mm thick sand layer to represent the drainage layer. A geogrid anchorage system ensured symmetry at the mid-length of the embankment by

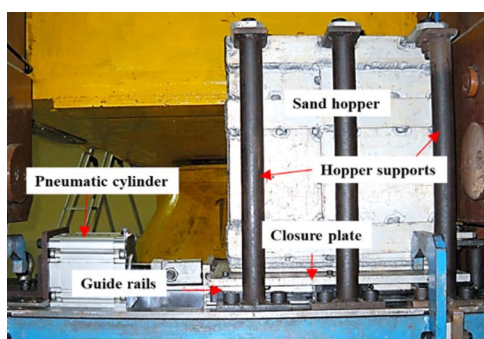**Fig. 3** Plan and elevation of the geogrid anchorage system
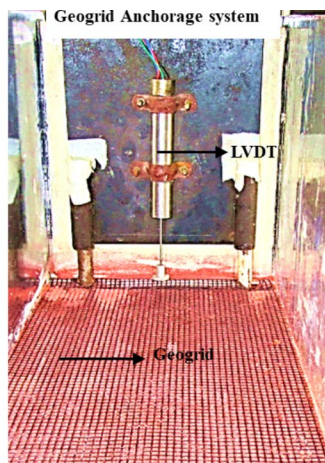
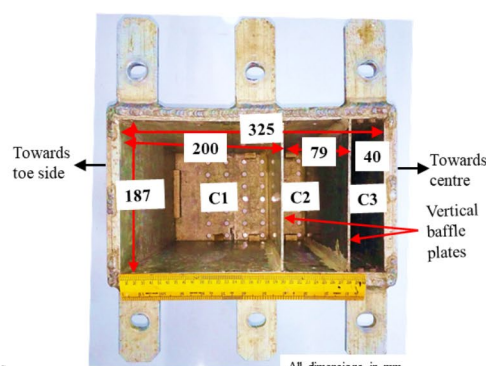(a) Geogrid anchorage system with LVDT fixed on the plate
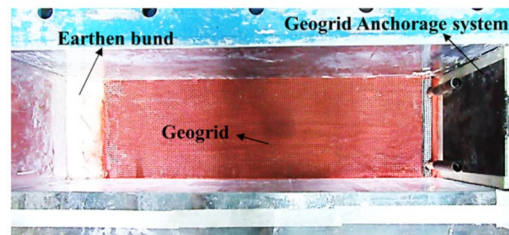
(b) Plan view of geogrid attached to geogrid anchorage system at the symmetrical end and earthen bund on the other side

Fig. 4 Sand hopper and its components

(a) Elevation of sand hopper mounted on the strong box with ancillaries

(b) Plan view of the sand hopper

allowing vertical movement of the geogrid at the centre. Figure 3 shows the plan and elevation views of the geogrid fixed to the anchorage system. The model was prepared in a strong box and was fitted with inflight sand hopper attachments like sand hopper, guide rails, closure plates, and hopper supports, as shown in Fig. 4.

The strong box was then loaded onto the swinging basket of the centrifuge. When the centrifuge reached the required gravity (40 g), the model was run at an angular velocity of 93 rpm for 10 min to allow the clay layer to settle under its own weight to simulate in situ stress conditions. The time-lapse mode of the camera was started to capture continuous photographs during embankment construction inflight. Figure 5 shows the schematic representation of the front elevation of the GRPE model at the end of embankment construction. As shown in Fig. 6, the model is subjected to rotation about a vertical axis in a horizontal plan with a velocity V and keeping that in view, directional vanes were inclined at about 35° with vertical. With this arrangement, the Coriolis effect could be minimized.

During in-flight, the embankment was constructed to a height of 150 mm, a crest width of 210 mm and a base width of 435 mm at a slope of 1 vertical to 1.5 horizontal. The variation in the prototype height of the embankment

with time during the centrifuge model tests is shown in Fig. 6. The time-lapse mode of the camera was turned off before the centrifuge was slowed. This plot indicates that the embankment construction could be completed in about 1.75 days on soft clay with and without geogrid supported pile inclusions. Currently, efforts are being made to slow down the ramping speed of the construction of the embankment at high gravity for the inflight sand hopper used in the present study.

Particle Image Velocimetry Technique

The particle image velocimetry technique (PIV) is an image-based deformation measurement technique that measures displacements in the form of contours and displacement vectors. It helps in the accurate determination of localised strain zones and improves the precision of strain measurements. The PIV measurement system includes image acquisition, data storage, communication, image analysis and support. The images are captured using the Canon Powershot A400 digital camera (USA make) affixed to a beam secured to the base plate positioned on the swinging basket of the centrifuge machine. Once the centrifugal acceleration

Fig. 5 Schematic representation of the front elevation of the GRPE test after embankment construction
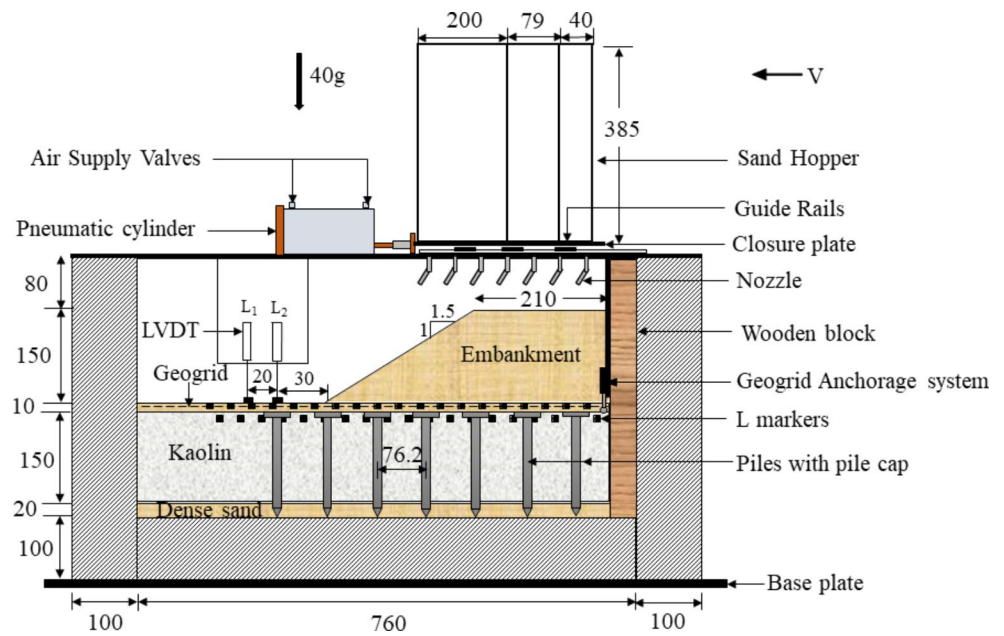

Fig. 6 Average rate of embankment construction in centrifuge model tests
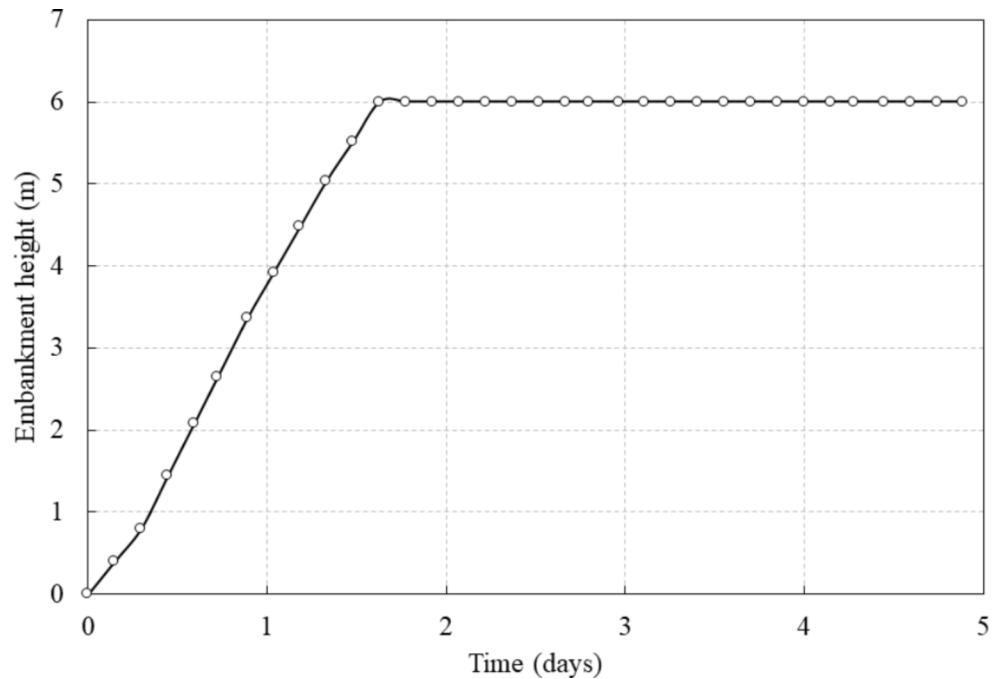

reaches a gravitational force of 40 g, the camera's time-lapse mode is activated. In this mode, the camera captures consecutive images at a resolution of 2046 × 1536 pixels, with a frame rate of 0.125 frames per second (fps). The digital images acquired during the testing were analysed using a digital image correlation software, Visual Image Correlation, in two dimensions (VIC-2D). The post-processing of the images in the present study was performed using a personal computer having Intel ® Core ™ i5-6500 3.20 GHz processing unit, 32 GB RAM and 64-bit operating system in five stages using VIC-2D version 6.0. The accuracy of this DIC system was evaluated by Khatami [59] to be 2×10^{-4} mm. Although Particle Image Velocimetry (PIV) serves as a valuable tool for comprehending deformation and strain patterns within subsoils, the precision of its outcomes hinges significantly upon factors such as speckle quality, light intensity, camera noise, and the selected subset size. To assess the accuracy of PIV-derived results, Fig. 7 shows the comparison of deformation profiles at the penultimate stage of the tests for the GR model. The results are compared with ImageJ software, which tracks the movement of markers positioned on the subsoil surface, and post-investigation

Fig. 7 Comparison of deformation profiles at the penultimate stage of centrifuge test for GR model
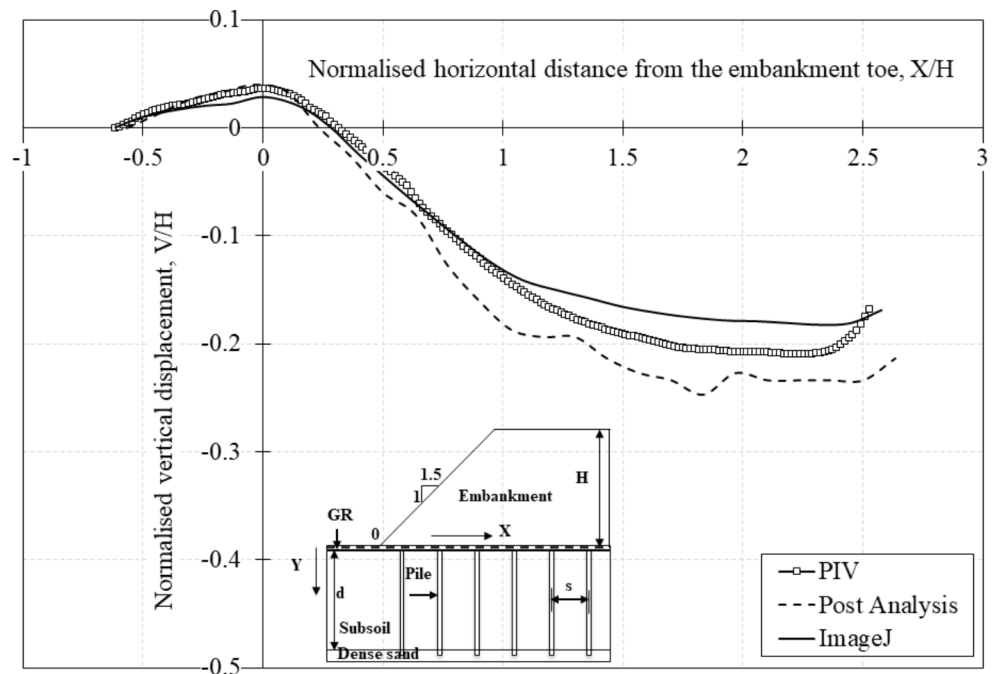
Fig. 8 Region of Interest of the image selected for PIV analysis and artificial seeding used for the study
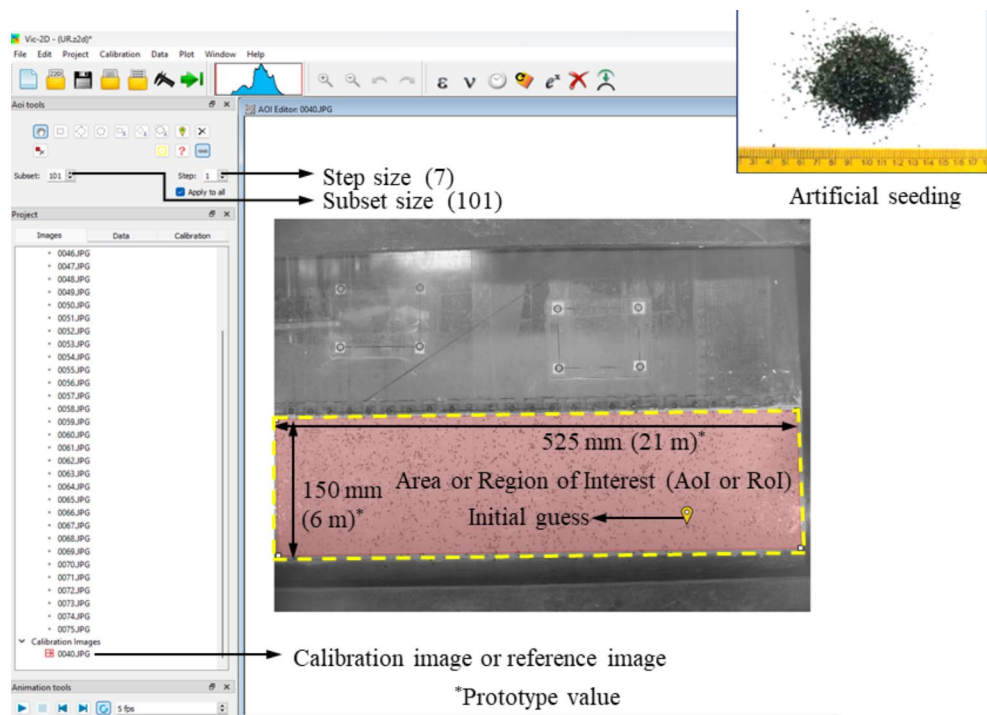
measurements acquired manually after test completion, involving the removal of soil and direct measurement using a scale. The figure indicates the robust capability of PIV in capturing deformation profile with good accuracy.

The steps involved in DIC analysis include adding a reference image, adding more speckle images, selecting the area of interest (AOI), selecting a calibrated scale, running the analysis and plotting the results. Square-shaped black tapes of 0.2 mm size were used as artificial seeding

for PIV analysis. An image at 40 g before the embankment construction is chosen as the reference image for the current study. Figure 8 shows the reference image and Area of Interest (AoI) selected for the current study. It is the area whose deformations are to be computed. The current study sets a rectangular area encompassing the foundation soil as the AoI. The entire AoI is subdivided into small square image patches known as subsets. Step size determines the frequency at which the data points are calculated. A

trial-and-error procedure has been used to fix the subset size and step size to achieve a standard error of 0·25 pixels, which is less than the prescribed value of 0·5 pixels in the GeoPIV-RG program for the geotechnical models [64]. A step size of 7 and a subset size of 101 was used for the current analyses.
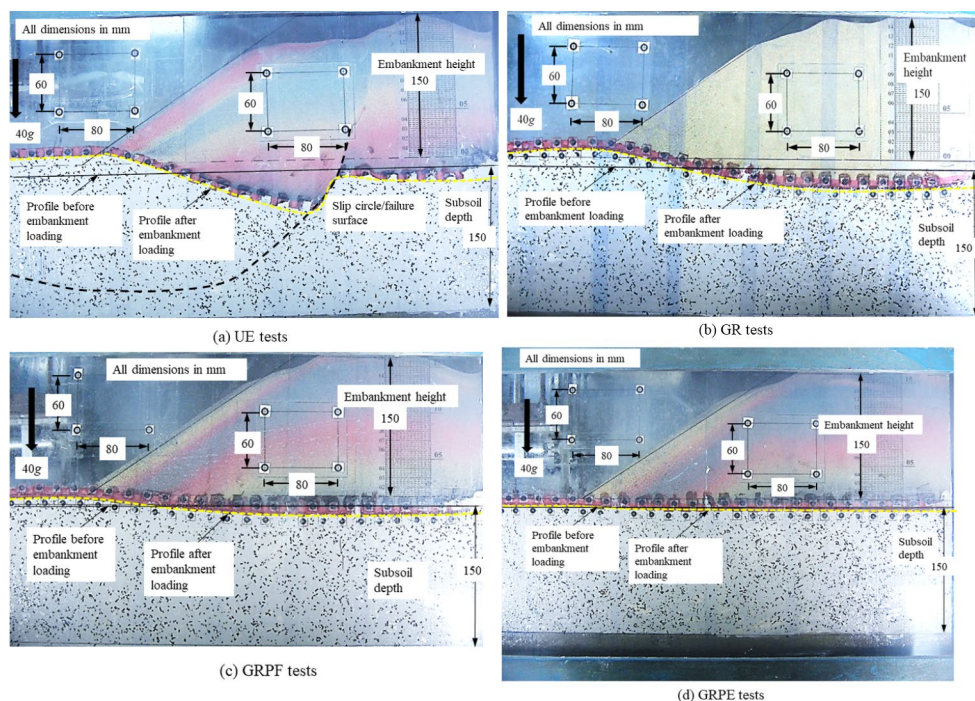
The embankment height was used as a reference to develop the scaling factor for the geometric details of the captured image. The calibrated scale adopted for all the tests is 1 px = 0.01 m. A point on the area at the bottom above the hard stratum and below the embankment centre was selected as the seed point for the current study for all the tests. After capturing speckle images, an analysis was performed by comparing them with a reference image to extract the displacement field. This involved using the Zero Normalised Square Differences (ZNSSD) correlation algorithm, which aligned subsets within the deformed and reference images. In VIC-2D, the default filter size is set to 15, which is considered suitable. The strain was calculated using the Lagrangian Strain Tensor method.

Results and Discussion

Deformation Behaviour and Contours During Embankment Construction

The deformations in different models at the end of embankment construction are shown in Fig. 9. The results are analysed based on the front elevation of the photographs captured in-flight by the onboard camera at their penultimate stage.

Unreinforced embankments underwent significant vertical and lateral displacements due to embankment loading followed by circular slip failure passing through the foundation soil at the end of embankment construction (Fig. 9a). The increase in vertical stress due to the embankment loading ($\Delta\sigma'_v$) at the bottom of the clay layer near the embankment centre is calculated as:

$$\Delta\sigma'_v = \gamma H I_f = 15.8 \times 6 \times 0.49 = 46.5\text{kPa} \tag{5}$$

where γ is the unit weight of the embankment fill, H is the embankment height, and I_f is the influence factor from the chart [60]. I_f is a function of B_1/z and B_2/z, where B_1 and B_2 are the crest width and embankment slope width, respectively, and z is the depth at which the vertical stress is computed. In the GR test, the inclusion of geogrid at the embankment base reduced the settlements and restrained the lateral movement due to the interlocking of particles with the geogrid. In contrast, model GRPF was observed to result in fewer settlements and heaving beyond the embankment toe. The rapid inflight embankment construction was completed within approximately 1.75 days. As can be seen Fig. 9d, there is not much variation in the final deformation profile from the initial profile in the case of the GRPE test. No heave was observed beyond the toe, and the model remained stable with the support from the hard strata. The settlement is reduced due to the added resistance from the end-bearing piles. This resistance is attributed to the reaction from stiff bearing strata given that the end-bearing piles rest on a firm stratum in the real scenario.

Fig. 9 Deformation profiles after embankment construction during the penultimate stage of centrifuge tests

Geogrid Strains from Marker-Based Analysis

The strain ε, experienced by the basal reinforcement sandwiched between the 20 mm drainage layer during embankment loading, was determined by tracking the movement of plastic markers glued to the geogrid layer during the model preparation from the digital images captured. The study utilised a method where the original length between markers was determined in the initial figure before embankment construction. Subsequent photographs were analysed to measure the changing distance between the same markers over time. The strain was calculated by dividing this change in length by the original distance, enabling a thorough analysis of geogrid strains throughout the entire embankment construction period. The strain developed between two movable markers along the geogrid reinforcement layer was calculated using the following equation:

$$\epsilon\,(\%) = 100 \times \sqrt{\frac{(x_2' - x_1')^2 + (y_2' - y_1')^2}{(x_2 - x_1)^2 + (y_2 - y_1)^2}} - 1 \qquad (6)$$

where (x_1, y_1), (x_2, y_2), are the initial coordinates of the two movable markers and (x_1', y_1'), (x_2', y_2'), are the coordinates of the displaced position of the movable markers. Figure 10 shows the variation of geogrid strain along the horizontal distance from the embankment toe for all the model tests at the end of embankment construction. The embankment toe is taken at a distance of 0 m in the graph.

When the embankment was reinforced with geogrid alone, the maximum strain of nearly 8% occurred near the embankment toe. At the toe, soil experienced maximum lateral deformations, and the GR underwent significant strain to restrain this movement. When embankments were reinforced with geogrids and floating piles, the maximum strain in the GR occurred at a normalised distance of 1.5 from the embankment toe. Large strain occurred at the midsection of the embankment, where the vertical load was higher for GRPF and GRPE tests. Compared with GRPE tests, the strain pattern was nearly the same, with a higher magnitude for GRPF tests. Larger strain values were found to occur near the edges of the pile cap for both GRPE and GRPF tests. Figure 11 shows the variation of geogrid strain with embankment height, which can be related to time. The geogrid strain had an M-shaped curve, as observed by [61]. The geogrid strain did not continuously increase with time. It increased initially, then decreased and increased again at nearly a normalised embankment height of 0.83. The strain in the GR increased with the embankment height. The magnitude of the mobilised tensile force was higher for GR tests, followed by GRPF tests. So, it is concluded that the tensioned membrane effect of geogrid reinforcement plays a more vital role in the load transfer mechanism of GRPF tests than the GRPE tests.
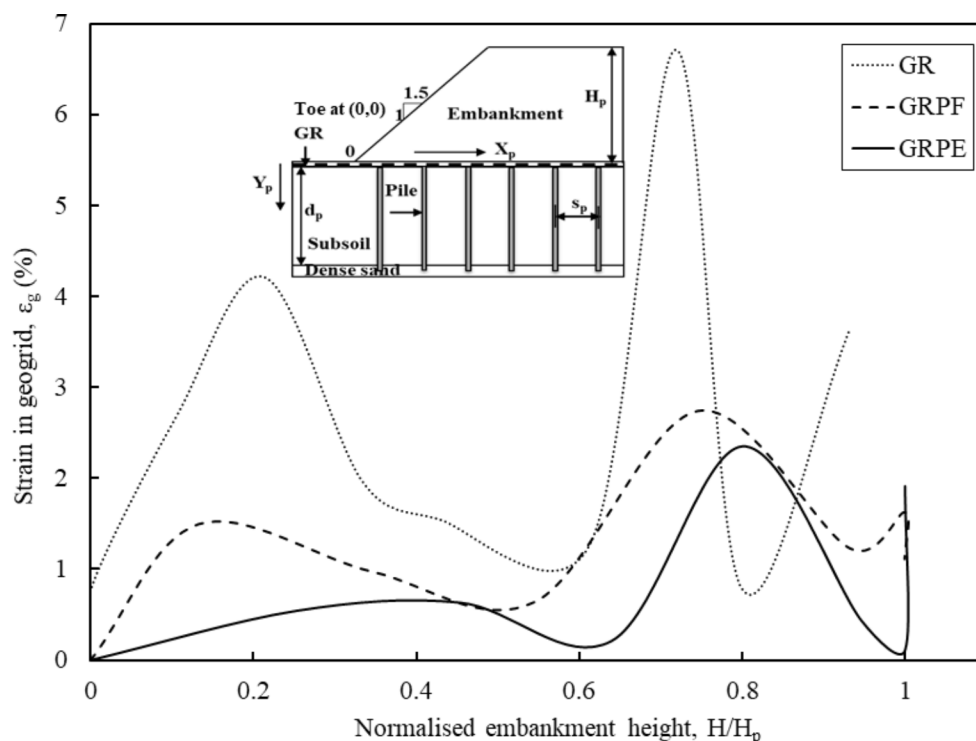
Distribution of Lateral Displacements

To investigate the failure mechanism and to visualise the extent and pattern of lateral spreading of soil, horizontal

Fig. 10 Geogrid strain profile for all the tests at the penultimate stage of the tests
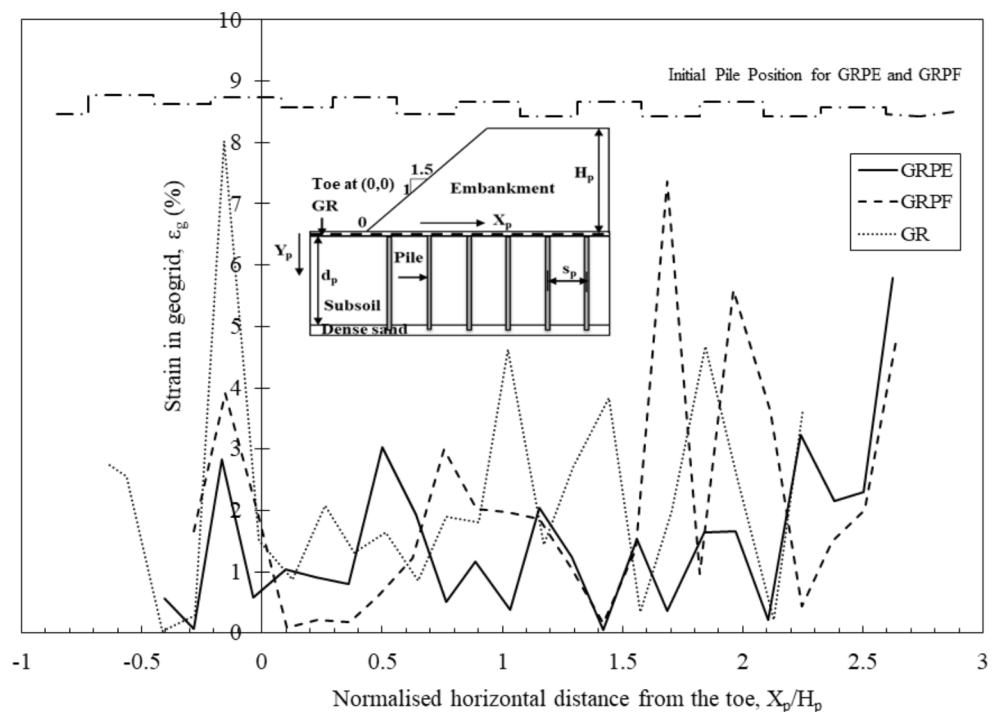
Fig. 11 Variation of geogrid strain with embankment height or loading

displacement contours were plotted for an unreinforced embankment, as shown in Fig. 12. The evolution of different deformation stages is depicted in the contour plots for certain embankment heights until the penultimate stage of the test. Figure 12 shows the formation of a global failure surface for an unreinforced embankment over soft clay, leading to a deep-seated rotational failure. This is evident clearly from Fig. 12d. The contours are shown in terms of the prototype scale.

In the case of an unreinforced embankment, lateral movements increased gradually from the embankment centre and reached a peak at about 6.5 m from the embankment toe. These displacements grew proportionally with the increase in the height of the embankment. When the embankment height reached 1.1 m, the maximum displacement contour shifted inward by about 0.2 m, forming a slip circle. With further height increase, the contour moved downward and towards the toe of the embankment. Horizontal displacements have reached maximum values at about 2 m below the ground surface. As the embankment height continued to increase, the maximum horizontal displacement significantly intensified, leading to embankment failure. Notably, minimal displacement was observed near the centre of the embankment.

Figures 13 and 14 compare the variation of normalised lateral displacementswith depth from the subsoil surface. Normalised lateral displacement (U_p/H_p) and normalised depth (d_p/H_p) are the lateral displacements and the depths normalised with the embankment height. The plots are

obtained by taking a vertical cross-section of the contour plots on the subsoil surface. During the progress of embankment construction, there had been an observed increase in the lateral movement of soil near the toe, as depicted in Fig. 14. A significant increase in the lateral movement occurs after 1.2 days, indicating a slope failure for the UE test. Unreinforced embankment experienced a maximum normalised lateral movement of nearly 0.3. Basal reinforcement enhances the lateral restraint, resulting in a reduction of lateral movement by approximately 50%. The inclusion of stiffer materials in the subsoil during the GRPF test results in a 53% reduction in lateral movement compared to GR test. The lateral movement is relatively small, measuring less than 0.05 when the piles are end-bearing in a hard stratum. A definite peak value in lateral movement was observed for unreinforced embankments. However, a definite peak value in lateral movement was not observed when reinforced embankments were supported with piles.

Distribution of Vertical Displacements

Figure 15 compares the variation of settlement at point 'A' on the foundation surface with time. Settlement increased linearly with time till the completion of construction at the end of 1.75 days. Thereafter, with constant embankment loading, settlement increased slowly. For the UE test, initial settlement occurred at a slower rate than for the GR tests, and after one day, there was a steady increase in settlement with a large magnitude, indicating slip-circle failure.
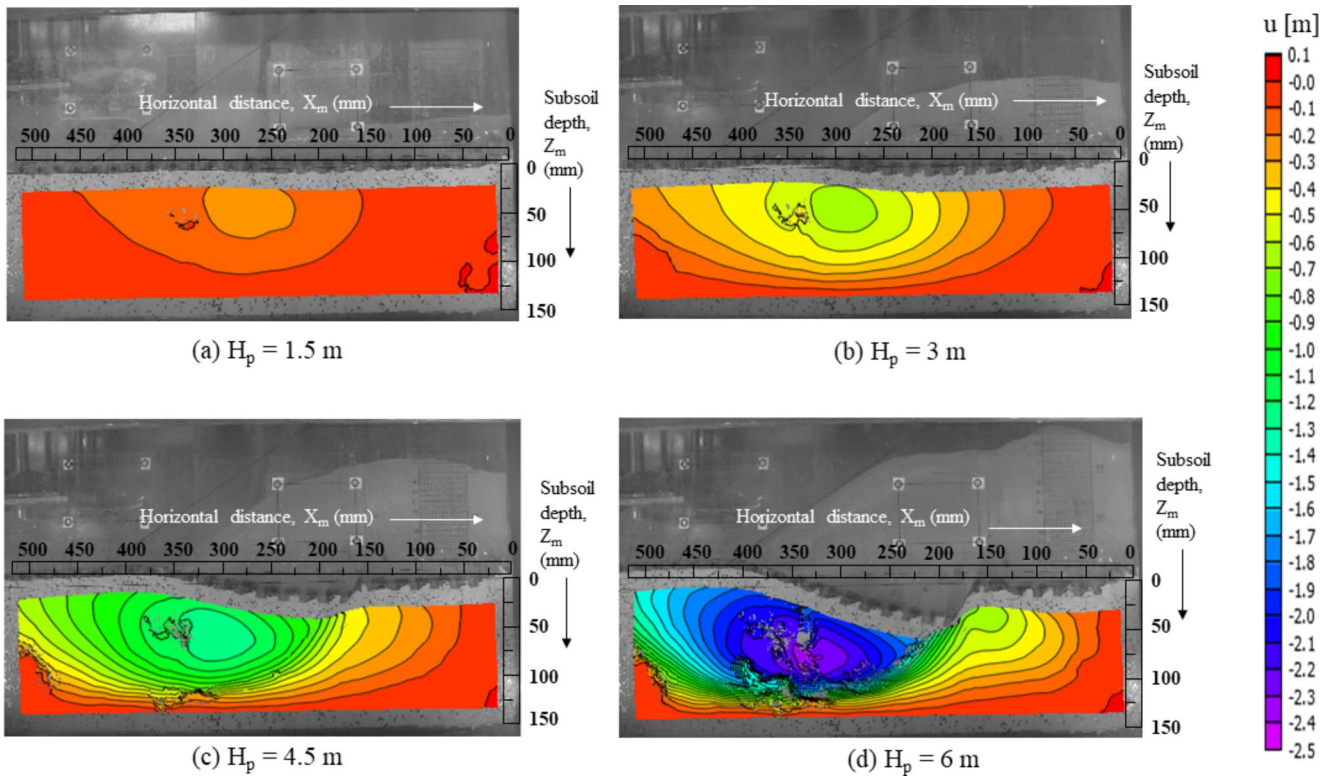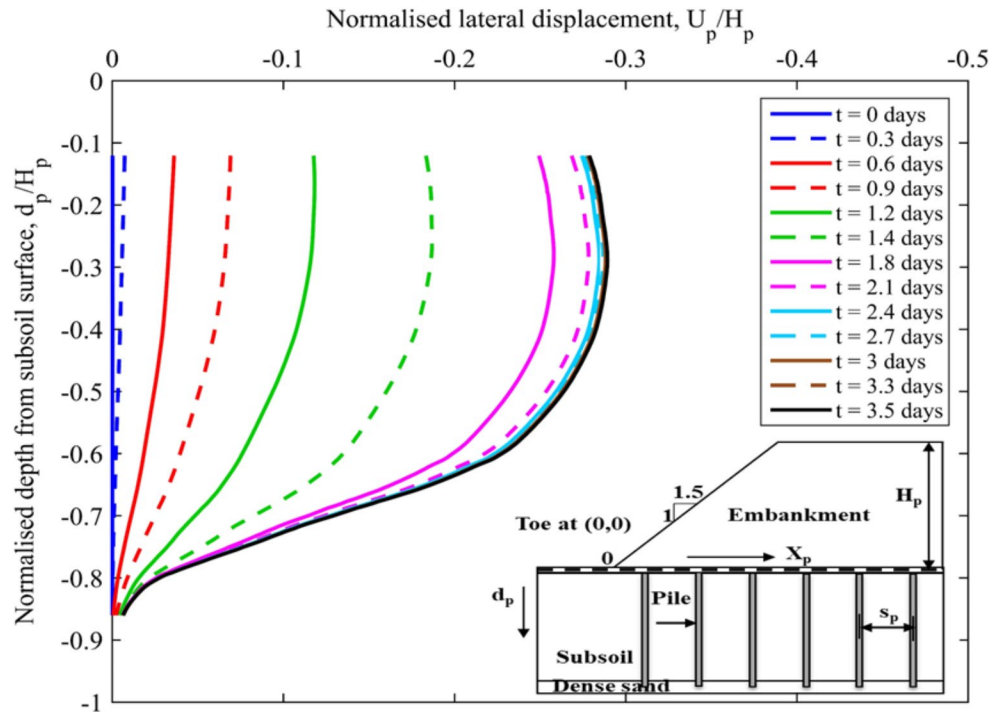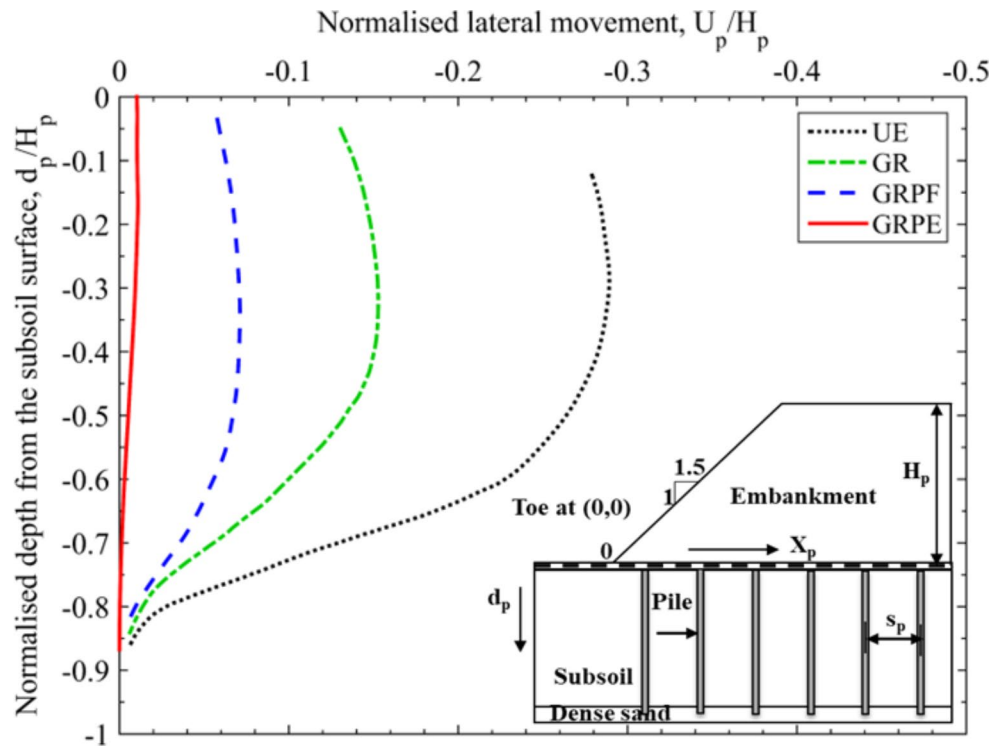
Fig. 12 Variation of horizontal displacement contours during centrifuge tests for UE test

Fig. 13 Variation of lateral displacement with depth for UE test during embankment construction

Fig. 14 Variation of lateral displacement with depth from the subsoil surface near the embankment toe during the penultimate stage of the centrifuge test at 40 g

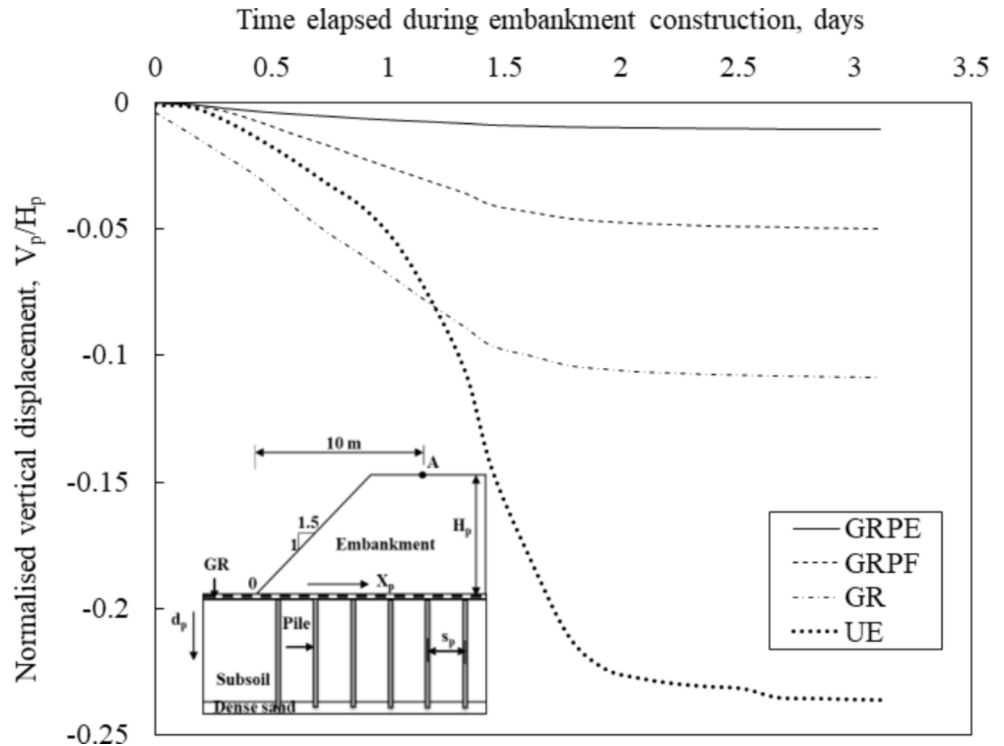**Fig. 15** Comparison of settlement-time graphs of all the tests

Figure 16 compares the variation of normalised vertical displacement V_p/H_p with normalised distance from the embankment toe X_p/H_p at the penultimate stage of the tests along different normalised depths from the subsoil surface d_p/H_p for GRPE and GRPF tests. The graphs were generated through PIV analyses, where cross-sections were taken at intervals of 1 m depth in prototype ($d_p/H_p = 0.17$). Positive displacement indicates heaving, and negative displacement indicates settlement. For the GRPE test at $d_p/H_p = 0$, undulations were seen in the vertical displacement. This is because the piles being stiff, displaced less when compared to the soil between the piles. The differential movement

Fig. 16 Variation of vertical displacement with distance from the centre of the embankment at the end of embankment construction at different depths below ground level

(a) GRPE test

(b) GRPF test
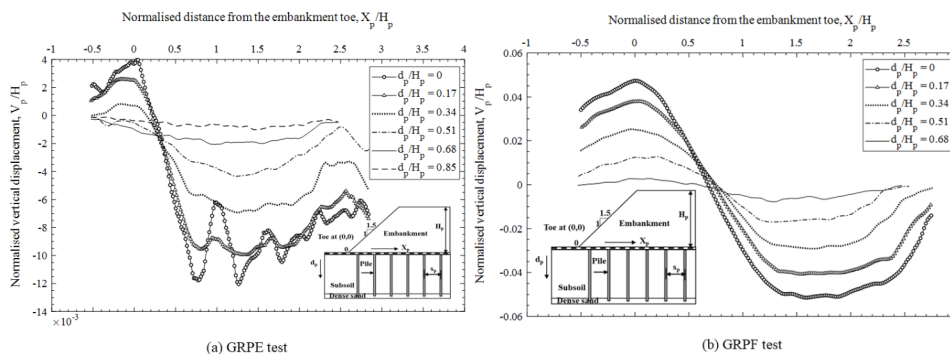
Fig. 17 Comparison of vertical displacement of all tests at the penultimate stage
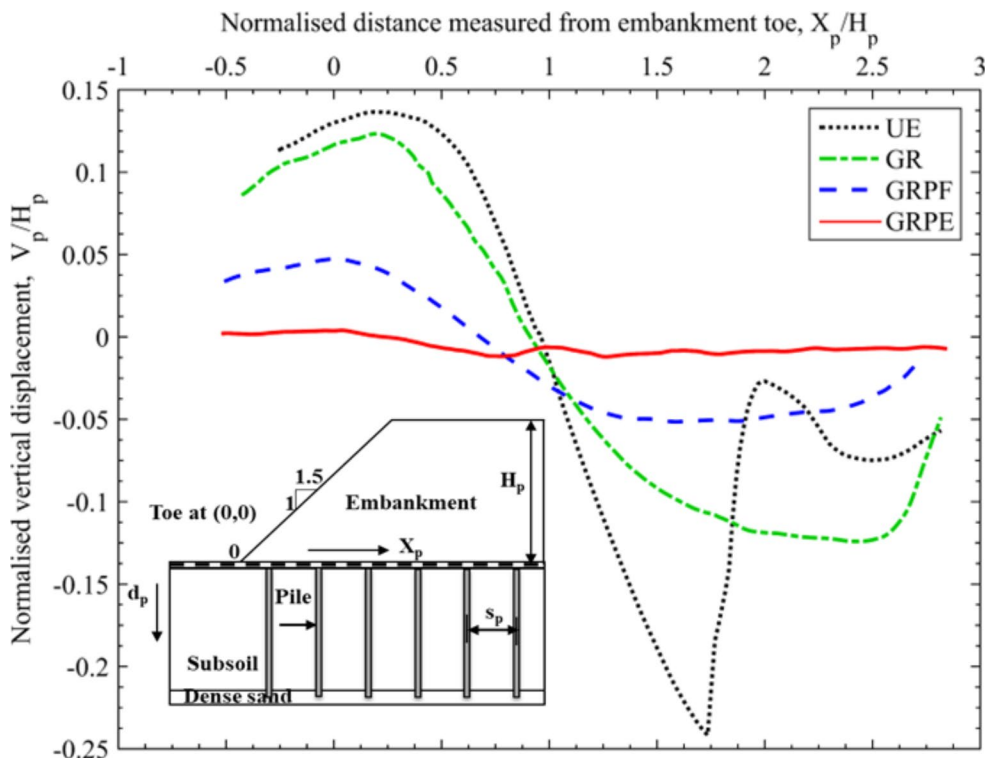
results in arching, which causes more load to be transferred to the stiffer piles. However, this was not observed in floating piles where the displacements appeared comparatively smoother. This is because floating piles did not have any resistance to the downward movement. It is inferred that negative skin friction or drag force is more common in the end-bearing piles in the GRPE test, causing larger differential settlement at the foundation surface compared to the floating piles in the GRPF test.

Figure 17 compares the variation of vertical displacement at the embankment surface with the distance from the embankment toe for all the tests at the end of embankment construction. The heave observed in UE and GR tests were nearly the same. There was only a 7% reduction in heave when geogrids were introduced at the base. However, the introduction of floating piles reduced the heave to 64%, and negligible heave was observed in the GRPE tests. The

Table 1 Comparison of PSR values of models at the penultimate stage

Sl No	Model	PSR
1	Geogrid Reinforced Embankments (GR)	51.7%
2	Geogrid Reinforced Embankments supported on Floating Piles (GRPF)	78.6%
3	Geogrid Reinforced Embankments supported on End-bearing Piles (GRPE)	95%

magnitude of settlement is quantified in terms of the Percentage Settlement Reduction factor (PSR) given by Eq. (7), and the values for different tests are given in Table 1.

$$PSR = 100 \times \left\{ \frac{S_{\max(unreinforced)} - S_{\max(reinforced)}}{S_{\max(unreinforced)}} \right\} \qquad (7)$$

From Fig. 17 in the unreinforced embankment (UE) test, notable concentrated settlements occurred, contrasting with other tests where settlements were dispersed across a

broader expanse. The anticipated maximum settlement is typically expected to occur at the centre of the embankment. However, it is important to note that the actual maximum settlement may deviate from the centre due to the high adhesion and friction between the clay soil and the surface of the wall, especially under higher gravitational forces.

Distribution of Shear Strains

The shear strain contours showing the failure mechanism for the UE test at different stages of embankment construction are shown in Fig. 18. The strain values are represented as unity and not as percentages in the contours. Shear strain distribution gives the mechanism of failure in the model tests. Shear strains are positive when the particles move in the direction of the applied force and negative when the particles move in the opposite direction to the applied force. For unreinforced embankments, when the height of the embankment was 1.5 m in the prototype, shear strain localisation was found at 3 m to 4 m from the embankment toe. These zones of strain localisation started moving towards the embankment toe with increasing height, and more zones of high shear strain started forming at deeper depths with an

increase in the embankment height. These pockets of maximum shear strain extended to the surface with an increase in load, leading to shear failure of the subsoil. A clear failure surface could be observed at the end of construction for unreinforced embankments due to progressive failure, and the shear zone was more localised into a narrow band. The magnitude of shear strains on the failure plane was more than 200%.

A comparison of shear strain contours of different tests at the penultimate stage is shown in Fig. 19. When the embankment was reinforced with a geogrid layer at the base, apart from reducing the magnitude of the shear strains, no stress concentrations were observed near the embankment base. This was because the basal reinforcement resisted the lateral deformation and changed the direction in which the shear stresses developed. However, at the end of the construction, a small area of stress concentration was observed at 4.5 m to 5.5 m from the embankment toe and a depth of 4.5 m from the top of the subsoil surface. For unreinforced embankments, shear strains changed the direction at a depth of 1.5 m to 2 m. This implied that particles near the surface moved downwards with the embankment height, and at a
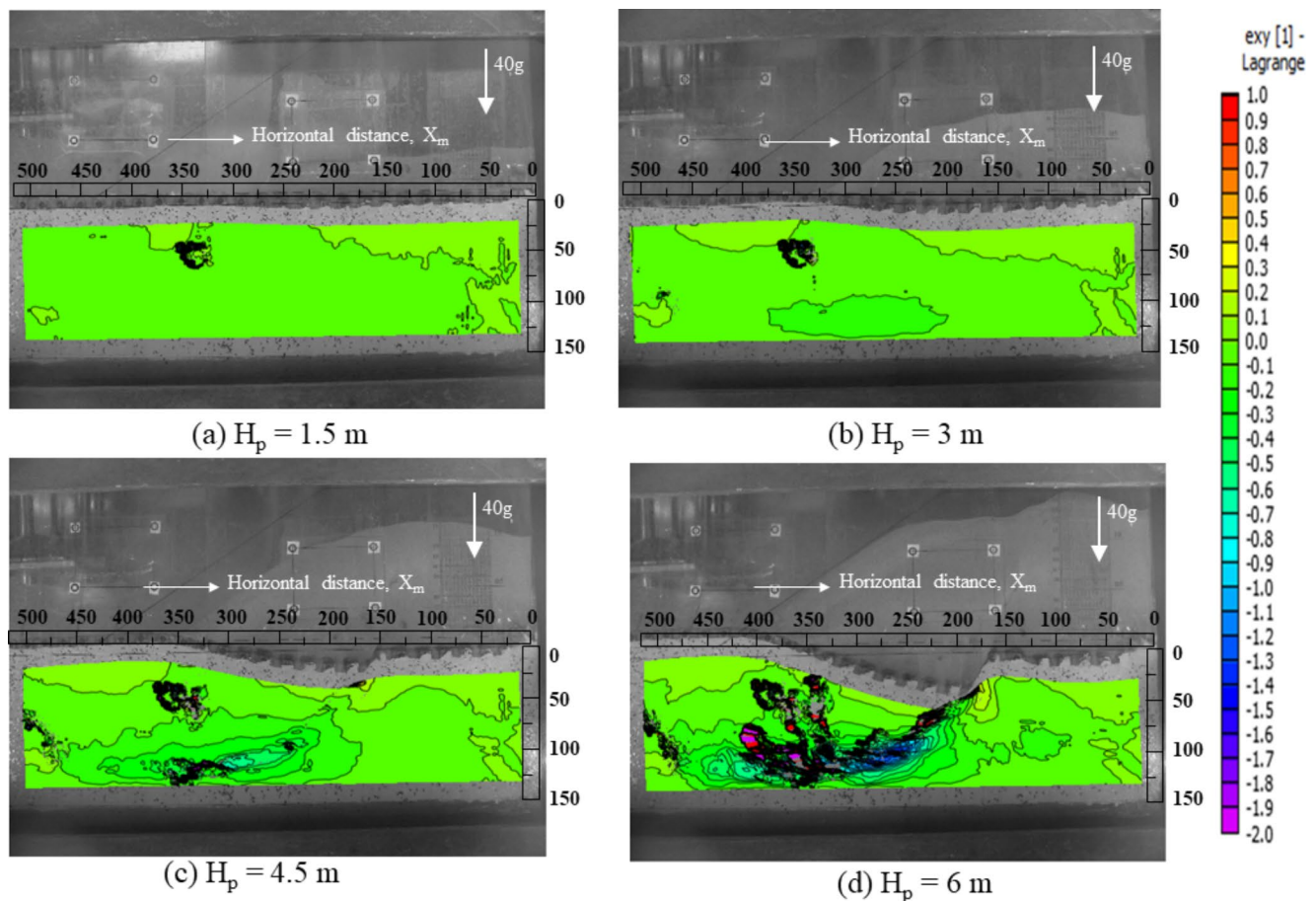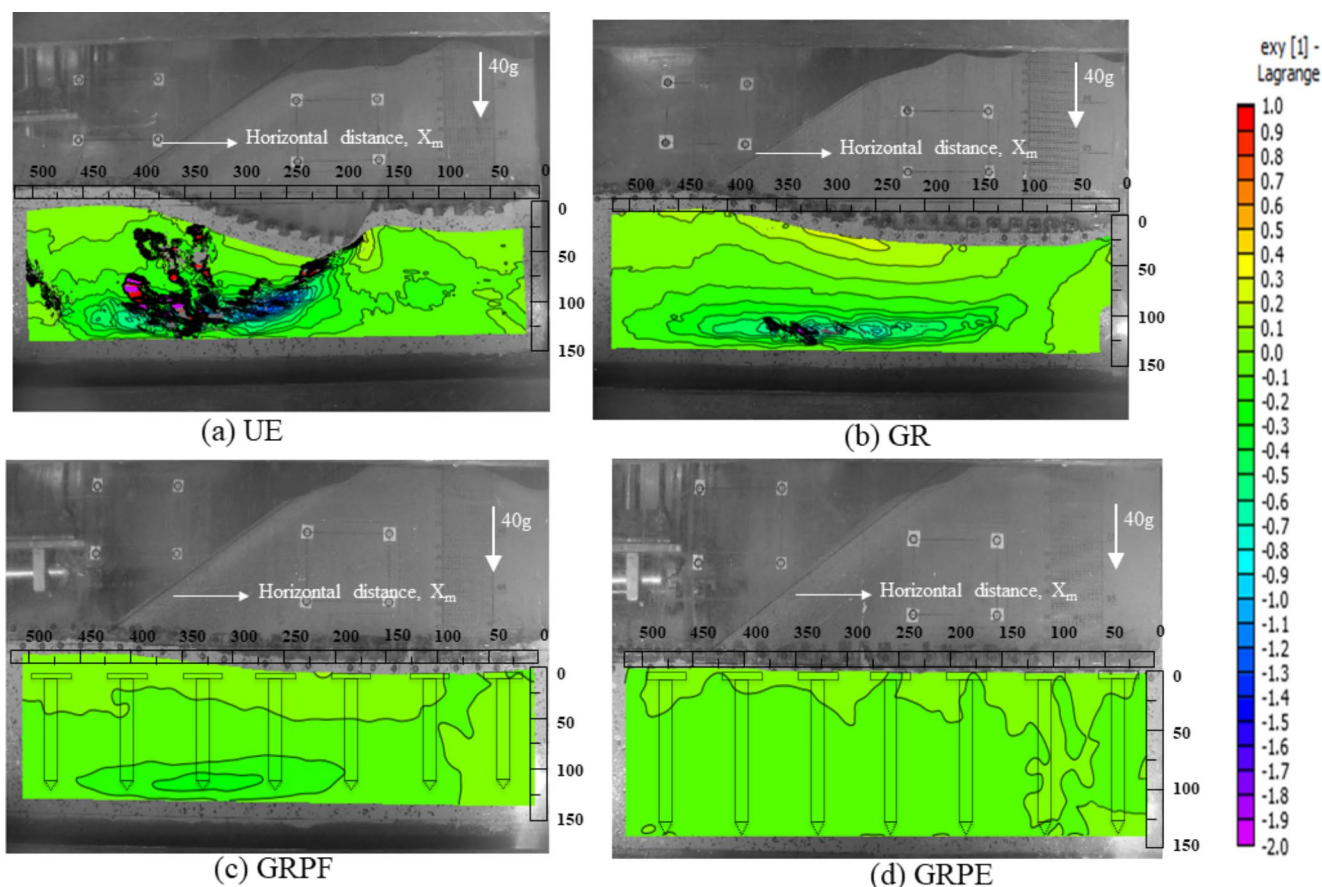

Fig. 18 Shear strain (%) variation with embankment heights for UE test

Fig. 19 Shear strain (%) variation for all the tests at the end of embankment construction

greater depth, the particles moved laterally outwards and upwards, causing the formation of slip surfaces and heaving.

When piles supported the embankment, the subsoil had no stress concentrations. When floating piles supported the basal reinforced embankments, shear strains of very low magnitude were observed at a depth of 4.5 m. For GRPF and GR tests, changes in the direction of shear strains were observed at 2.2 m and 2.4 m, respectively. However, for GRPE, shear strains were nearly zero and were more concentrated near the embankment surface.

Post-Investigation of the Data

After the termination of centrifuge model tests, post-investigation analysis was carried out to inspect the cracks that developed along the surface of the soft subsoil. It has been assumed that the behaviour of embankments under soft clay is perfectly undrained during construction, and drainage starts only after construction. The dry drainage layer was found to be wet post-investigation in all the tests. There was some partial drainage during the embankment construction.

For GR tests, geogrid reinforcement came out of place beyond the embankment toe, as shown in Fig. 20. This was due to the heaving of the soil beyond the toe of the embankment, as there is very low confinement for the geogrid.

The container was disassembled for GRPF and GRPE tests, and the clay layer was cut open. The pile cap was carefully removed by unscrewing, and the profile of the piles was observed.

Figures 21 and 22 show the failure mechanism of geogrid-reinforced embankments supported on piles. It was inferred that the lateral failure of piles was the primary failure mode for such embankments compared to sudden slip circle failure. From the observations, the amount of inclination varies with the pile positions. For GRPE tests, piles near the mid-section of the embankment, specifically piles 7 and 5, showed minimal displacement under embankment load, as seen in Fig. 22. The pile tip at the mid-section of embankment exhibited outward movement toward the embankment toe, while those near the embankment toe displayed inward movement. Further analysis of GRPF piles revealed a failure mode characterized by a combination of punching and rotation or tilting. Notably, the inclination angle of pile 13 near the toe in GRPF tests exceeded that observed in GRPE
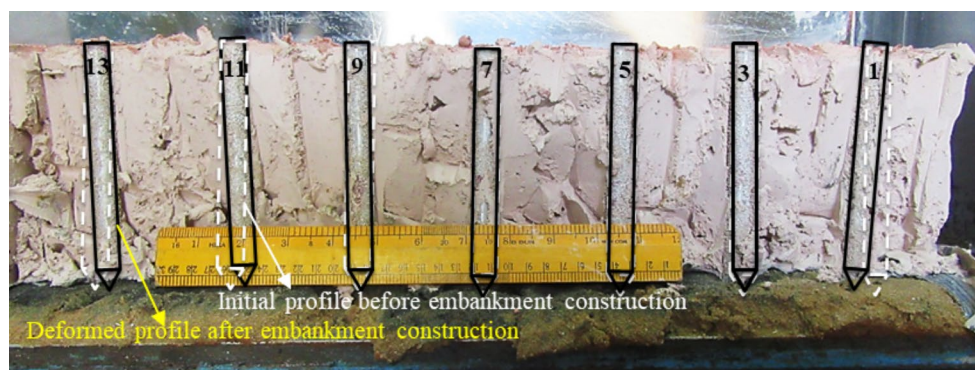
Fig. 20 Plan view of geogrid reinforcement as observed after GR test
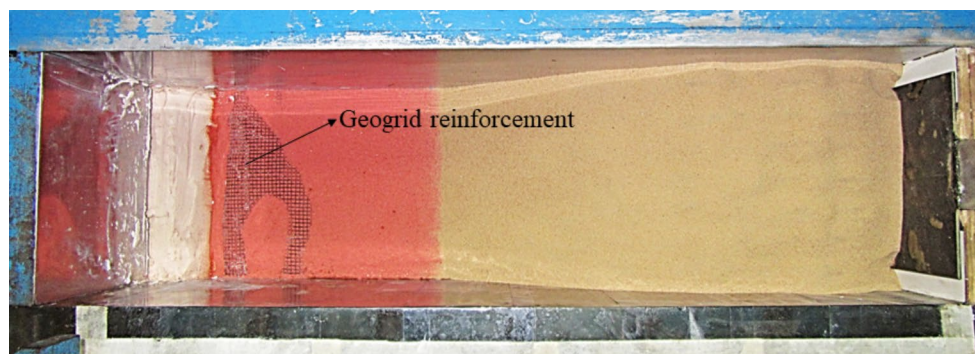
Fig. 21 Deflection of the piles in GRPF test observed during post-investigation
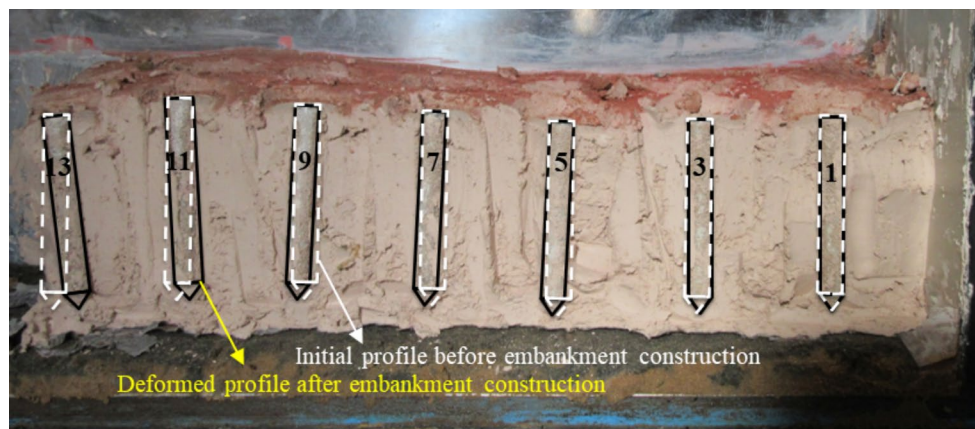
Fig. 22 Deflection of the piles in GRPE test observed during post-investigation

tests. Deflection patterns for GRPF piles near the mid-section of the embankment remained limited, while those near the toe moved inward toward the embankment centre, as illustrated in Fig. 21. Thus, it can be inferred that failure initiation likely begins with piles near the embankment toe.

Limitations of the Study

While centrifuge model tests provide a controlled environment to simulate real-world conditions, they have certain limitations. In general, the errors that arise when subjecting a model to a higher gravitational field include (i) Variation of gravity level with depth and horizontal distance in the model, (ii) Non-linear variation of vertical stresses, (iii)

Coriolis effect, and (iv) boundary and particle size effects. Limitations from the present study include: (i) The embankment was constructed inflight, but the installation of piles at normal gravities may have influenced the results. (ii) the subsoil was not pre-consolidated and hence, the results pertain to only normally consolidated foundation soils. Specialized instrumentation, like earth pressure sensors and strain gauges on geogrids and piles, is required for a better understanding of the load-transfer mechanism. Despite the inherent limitations of the centrifuge modelling, researchers such as Mitchell [62] have advocated its use as a consulting tool to enhance the understanding of stability and settlement issues associated with embankments.

Conclusions

The principal aim of this investigation is to understand the deformation characteristics of soft subsoil subjected to an embankment loading with and without reinforcement and supported with piles of different bearing types. The study explained the working of an inflight sand hopper to construct an embankment to a height of 6 m at 40 times the gravity at a slope inclination of 37° with the horizontal. Based on the analysis and interpretation of test results, it can be concluded that:

1. The unreinforced embankments experience significant vertical and lateral displacement subjected to inflight loading followed by a deep-seated circular failure at a normalised embankment height of 0.6, which could be attributed to the low shear strength of the foundation soil. Maximum lateral movements were observed near the embankment toe.

2. Geogrid reinforcement at the base reduced lateral spreading near the embankment toe by 50% through interlock and friction mechanisms. Maximum strain in the geogrid layer was observed near the embankment toe where significant lateral deformations have taken place. The shear strain pattern indicated that the basal reinforcement layer has effectively reduced the shear strain concentrations near the base, altering the direction of shear stress development.

3. Using floating piles reduced the settlement and heaving beyond the toe compared to GR test. Geogrid strain analysis showed higher magnitude near the mid-section of the embankment indicating effective load transfer and restraint provided by the piles. The lateral movement was significantly reduced, with a 53% reduction compared to GR tests.

4. The GRPE test showed the least variation in final deformation profile with no heave observed beyond the embankment toe indicating enhanced stability. The added resistance from the end-bearing piles resting on a hard stratum has minimized the settlements. The shear strain contours indicated minimal stress concentrations, with shear strains concentrated near the embankment surface.

5. Differential settlements were observed at the ground surface during the penultimate stage of the GRPE test but not in the GRPF test at the same embankment height. This pattern of soil displacements suggests increased arching for end-bearing piles compared to floating piles.

6. Post-investigation studies suggest that the geogrid-reinforced pile-supported embankments experience gradual pile failure rather than sudden shear failure seen in unreinforced embankments. Specifically, GRPF piles demonstrate a combination of punching and rotation or tilting failure, exhibiting lesser stability than GRPE, with higher tilt observed for the piles near the embankment toe in GRPF tests.

The PIV application facilitated comprehension of subsoil deformation behaviour under embankment loading and visualized the failure mechanisms for unreinforced embankments. Further research is needed to assess the impact of basal reinforcement compared to conventional piled embankments and to understand the effects of pile spacing and the stiffness of the basal reinforcement on deformation behaviour. In conclusion, this study underscores the efficacy of PIV in understanding the deformation characteristics of soft clays during rapid construction with varying embankment heights.

Declarations

References

1. Chen RP, Xu ZZ, Chen YM et al (2010) Field tests on pile supported embankments over soft ground. J Geotech Geoenvironmental Eng ASCE 136(6):777–785. https://doi.org/10.1061/(ASCE)GT.1943-5606.0000295

2. van Eekelen SJM, Han J (2020) Geosynthetic-reinforced pile-supported embankments: state of the art. Geosynthetics Int 27(2):112–141. https://doi.org/10.1680/jgein.20.00005

3. Bhasi A, Rajagopal K (2015) Numerical study of basal reinforced embankments supported on floating/end bearing piles considering pile–soil interaction. Geotext Geomembr 43(6):524–536

4. van Eekelen SJM, Bezuijen A, van Tol AF (2013) An analytical model for arching in piled embankments. Geotext Geomembr 3978–3102. https://doi.org/10.1016/j.geotexmem.2013.07.005

5. BS 8006-1:2010 (2010) Code of practice for strengthened / reinforced soils and other fills. BSI Stand Publication 179–191

6. Bräu G, Herold A, Lüking J, Naciri O (2010) EBGEO 2010 - Recommendation for reinforcement with geosynthetics. In: 9th International Conference on Geosynthetics. Brazil, pp 233–236

7. Rogbeck Y, Alén C, Franzén G et al (2004) Nordic guidelines for Reinforced soils and fills. The Nordic Geotechnical Societies

8. CUR226 (2016) Design Guideline - basal Reinforced Piled embankments. Revision of the Design Guideline CUR226. SBRCURnet & CRC, Delft, Netherlands

9. Diao Y, Ren H, Jia Z et al (2023) A simplified method for progressive failures of piles in soft ground during rapid embankment construction. Comput Geotech 153(July 2022):105076. https://doi.org/10.1016/j.compgeo.2022.105076

10. Zheng G, Yang X, Zhou H, Chai J (2019) Numerical modeling of progressive failure of rigid piles under embankment load. Can Geotech J 56(1):23–34. https://doi.org/10.1139/cgj-2017-0613

11. Taha A, Naggar MHE, Turan A (2014) Experimental and numerical study on lateral behaviour of geosynthetic-reinforced pile foundation system. Geosynthetics Int 21(6):352–363. https://doi.org/10.1680/gein.14.00023

12. Wang A, Zhang D (2020) Lateral response and failure mechanisms of rigid piles in soft soils under geosynthetic-reinforced embankment. Int J Civil Eng 18(2):169–184. https://doi.org/10.1007/s40999-019-00434-1

13. Almeida MSS, Ehrlich M, Spotti AP, Marques MES (2007) Embankment supported on piles with biaxial geogrids. Proc Institution Civil Eng - Geotech Eng 160(4):185–192. https://doi.org/10.1680/geng.2007.160.4.185

14. Briançon L, Simon B (2012) Performance of pile-supported embankment over soft soil: full-scale experiment. J Geotech Geoenvironmental Eng ASCE 138(4):551–561. https://doi.org/10.1061/(ASCE)GT.1943-5606.0000561

15. Zhuang Y, Cui XY (2016) Case studies of Reinforced Piled High-Speed Railway Embankment over Soft soils. Int J Geomech 16(2):6015005. https://doi.org/10.1061/(ASCE)GM.1943-5622.0000519

16. King DJ, Bouazza A, Gniel JR et al (2017) Serviceability design for geosynthetic reinforced column supported embankments. Geotext Geomembr 45(4):261–279. https://doi.org/10.1016/j.geotexmem.2017.02.006

17. van Eekelen SJM, Venmans AAM, Bezuijen A, van Tol AF (2020) Long term measurements in the Woerden geosynthetic-reinforced pile-supported embankment. Geosynthetics Int 27(2):142–156. https://doi.org/10.1680/jgein.17.00022

18. Xu C, Song S, Han J (2016) Scaled model tests on influence factors of full geosynthetic-reinforced pile-supported embankments. Geosynthetics Int 23(2):140–153. https://doi.org/10.1680/jgein.15.00038

19. Kongkitkul W, Chaiyaporn U, Youwai S, Jongpradist P (2012) Role of geogrids in load transfer of pile-supported embankments. Proc Inst Civil Eng Ground Improv 165(4):239–248. https://doi.org/10.1680/grim.11.00019

20. Fonseca ECA, Palmeira EM, Barrantes MV (2018) Load and deformation mechanisms in Geosynthetic-Reinforced piled embankments. Int J Geosynthetics Ground Eng 4(32). https://doi.org/10.1007/s40891-018-0150-x

21. Blanc M, Rault G, Thorel L, Almeida M (2013) Centrifuge investigation of load transfer mechanisms in a granular mattress above a rigid inclusions network. Geotext Geomembr 3692–3105. https://doi.org/10.1016/j.geotexmem.2012.12.001

22. Fagundes DF, Almeida MSS, Thorel L, Blanc M (2017) Load transfer mechanism and deformation of reinforced piled embankments. Geotext Geomembr 45(2):1–10. https://doi.org/10.1016/j.geotexmem.2016.11.002

23. Feng S, Xu R, Cheng K et al (2020) Centrifuge model test on the performance of Geogrid-Reinforced and Pile-supported embankment over soft soil. Soil Mech Found Eng 57(3):244–251. https://doi.org/10.1007/s11204-020-09661-4

24. Shen P, Xu C, Han J (2020) Geosynthetic-reinforced pile-supported embankment: settlement in different pile conditions. Geosynthetics Int 27(3):315–331. https://doi.org/10.1680/jgein.19.00015

25. Yu Jlin, Zhou Jjin, Gong X, nan et al (2021) Centrifuge study on behavior of rigid pile composite foundation under embankment in soft soil. Acta Geotech 16(6):1909–1921. https://doi.org/10.1007/s11440-020-01109-1

26. Xie M, Li L, Cao W et al (2023) Centrifugal and numerical modeling of embankment widening over soft soils treated by pile-supported geosynthetic-reinforced soil wall. Acta Geotech 18(2):829–841. https://doi.org/10.1007/s11440-022-01611-8

27. Girout R, Blanc M, Thorel L, Dias D (2018) Geosynthetic reinforcement of pile-supported embankments. Geosynthetics Int 25(1):37–49. https://doi.org/10.1680/jgein.17.00032

28. King L, Bouazza A, Gaudin C et al (2019) Behavior of Geosynthetic-Reinforced piled embankments with defective piles. J Geotech Geoenvironmental Eng ASCE 145(11). https://doi.org/10.1061/(asce)gt.1943-5606.0002125

29. Huat BBK, Ali FH, Pile Embankment on Soft Clay : Comparison Between Model and Field Performance. In: Third International Conference on Case Histories in Geotechnical Engineering

30. Saboya F, Tibana S, Reis RM et al (2021) Centrifuge modeling of Soft Soil Reinforced with Granular columns. Geotech Geol Eng 39(4):2955–2967. https://doi.org/10.1007/s10706-020-01671-1

31. Davies MCR (1985) TN17. Centrifuge model of an embankment failure. Failures in Earthworks. Thomas Telford Publishing, pp 451–453

32. Allersma HGB, Ravenswaay L, Vos E (1994) Investigation of road widening on soft soils using a small centrifuge. Transp Res Rec (1462):47–53

33. Stuit HG (1995) Sand in the Geotechnical Centrifuge. Delft University of Technology

34. Zheng G, Xia B, Zhou H et al (2023) Centrifuge modelling of the progressive failure of geosynthetic-reinforced embankments. Geosynthetics International 1–14. https://doi.org/10.1680/jgein.23.00061

35. Fretti C, Presti DL, Pedroni S (1995) A pluvial deposition method to reconstitute well-graded sand specimens. Geotech Test J 18(2):292–298

36. Madabhushi SPG, Haigh SK, Houghton NE (2006) A new CNC sand pourer for model preparation at University of Cambridge. In: Proceedings of the 6th International Conference on Physical Modelling in Geotechnics. Balkema, Hong Kong, pp 217–222

37. Detert O, König D, Schanz T (2012) Centrifuge modeling of an adaptive foundation system for embankments on soft soils. Geotechniek 16(4):46–54

38. Hussain AD (2010) Design and fabrication of In-flight sand hopper. Indian Institute of Technology Bombay

39. Gerber E (1929) Untersuchungen uber die Druckverteilung im Oertlick Belasteten Sand. Dissertation Technische Hochschule, Zurich

40. Sadek S, Iskander MG, Liu J (2003) Accuracy of Digital Image Correlation for Measuring Deformations in transparent media. J Comput Civil Eng ASCE 17(2):88–96. https://doi.org/10.1061/(ASCE)0887-3801(2003)17:2(88)

41. White DJ, Bolton MD (2004) Displacement and strain paths during plane-strain model pile installation in sand. Géotechnique 54(6):375–397. https://doi.org/10.1680/geot.2004.54.6.375

42. Stanier SA, Black JA, Hird CC (2012) Enhancing accuracy and precision of transparent synthetic soil modelling. Int J Phys Modelling Geotechnics 12(4):162–175. https://doi.org/10.1680/ijpmg.12.00005

43. Take WA (2015) Thirty-Sixth Canadian Geotechnical Colloquium: advances in visualization of geotechnical processes through digital image correlation. Can Geotech J 52(9):1199–1220. https://doi.org/10.1139/cgj-2014-0080

44. Gedela R, Kalla S, Sudarsanan N, Karpurapu R (2021) Assessment of load distribution mechanism in geocell reinforced foundation beds using Digital Imaging correlation techniques. Transp Geotechnics 31(September):100664. https://doi.org/10.1016/j.trgeo.2021.100664

45. Chen J, RS CMAR, TRN (1996) An evaluation of three different image capture methods for measurement and analysis of deformation within a geotechnical centrifuge. Int Archives Photogrammetry Remote Sens 31(B5):70–75

46. Viswanadham BVS, König D (2009) Centrifuge modeling of geotextile-reinforced slopes subjected to differential settlements. Geotext Geomembr 27(2):77–88. https://doi.org/10.1016/j.geotexmem.2008.09.008

47. Zhang G, Hu Y, Zhang JM (2009) New image analysis-based displacement-measurement system for geotechnical centrifuge modeling tests. Measurement: J Int Meas Confederation 42(1):87–96. https://doi.org/10.1016/j.measurement.2008.04.002

48. Stanier SA, White DJ (2013) Improved image-based deformation measurement in the centrifuge environment. Geotech Test J 36(6):915–928. https://doi.org/10.1520/GTJ20130044

49. Divya PV, Viswanadham BVS, Gourc JP (2017) Centrifuge modeling and digital image cross-correlation analysis of geofiber-reinforced clay-based landfill covers. J Geotech Geoenvironmental Eng ASCE 143(1):04016076–04016071. https://doi.org/10.1061/(ASCE)GT.1943-5606.0001563

50. White DJ, Take WA (2005) Discussion on application of particle image velocimetry (PIV) in centrifuge testing of uniform clay. Int J Phys Modelling Geotechnics 5(4):27–31

51. Reshma B, Rajagopal K, Viswanadham BVS (2020) Centrifuge model studies on the settlement response of geosynthetic piled embankments. Geosynthetics Int 27(2):170–181. https://doi.org/10.1680/jgein.19.00009

52. Stanier SA, Blaber J, Take WA, White DJ (2015) Improved image-based deformation measurement for geotechnical applications. Can Geotech J 1–35

53. Chandrasekaran V (2001) Numerical and centrifuge modelling in soil struture interaction. Indian Geotech J 31(1):30–59

54. Viswanadham BVS, König D (2004) Studies on scaling and instrumentation of a geogrid. Geotext Geomembr 22(5):307–328. https://doi.org/10.1016/S0266-1144(03)00045-1

55. Balakrishnan S, Viswanadham BVS (2016) Performance evaluation of geogrid reinforced soil walls with marginal backfills through centrifuge model tests. Geotext Geomembr 44(1):95–108. https://doi.org/10.1016/j.geotexmem.2015.06.002

56. Izawa J, Kuwano J (2010) Centrifuge modelling of geogrid reinforced soil walls subjected to pseudo-static loading. Int J Phys Modelling Geotechnics 10(1):1–18. https://doi.org/10.1680/ijpmg.2010.10.1.1

57. Rao SN, Prasad YVSN (1993) Estimation of uplift capacity of helical anchors in clays. J Geotech Eng ASCE 119(2):352–357

58. Madabhushi G (2014) Centrifuge modelling for civil engineers. CRC Press, Taylor & Francis group

59. Khatami H, Deng A, Jaksa M (2019) An experimental study of the active arching effect in soil using the digital image correlation technique. Comput Geotech 108183–108196. https://doi.org/10.1016/j.compgeo.2018.12.023

60. Osterberg JO (1957) Influence values for vertical stresses in a semi-infinite mass due to an embankment. Proceedings of the 4th international conference on soil mechanics and foundation engineering 1393–394

61. Shen P, Xu C, Han J (2020) Centrifuge tests to investigate global performance of geosynthetic-reinforced pile-supported embankments with side slopes. Geotext Geomembr 48(1):120–127. https://doi.org/10.1016/j.geotexmem.2019.103527

62. Mitchell RJ (1991) Centrifuge modelling as a consulting tool. Can Geotech J 28(1):162–167. https://doi.org/10.1139/t91-018